Batteries & Supercaps

Supporting Information

Fast Charge and High Stability of Solid-State Graphite Organic Ionic Plastic Crystal Composite Anodes

Hiroyuki Ueda,* Fuminori Mizuno, Robert Kerr, Maria Forsyth, and Patrick C. Howlett*

Supporting Information

Contents

Supporting Information

I. Supporting artworks for the "*Initial charge-discharge profile*" section

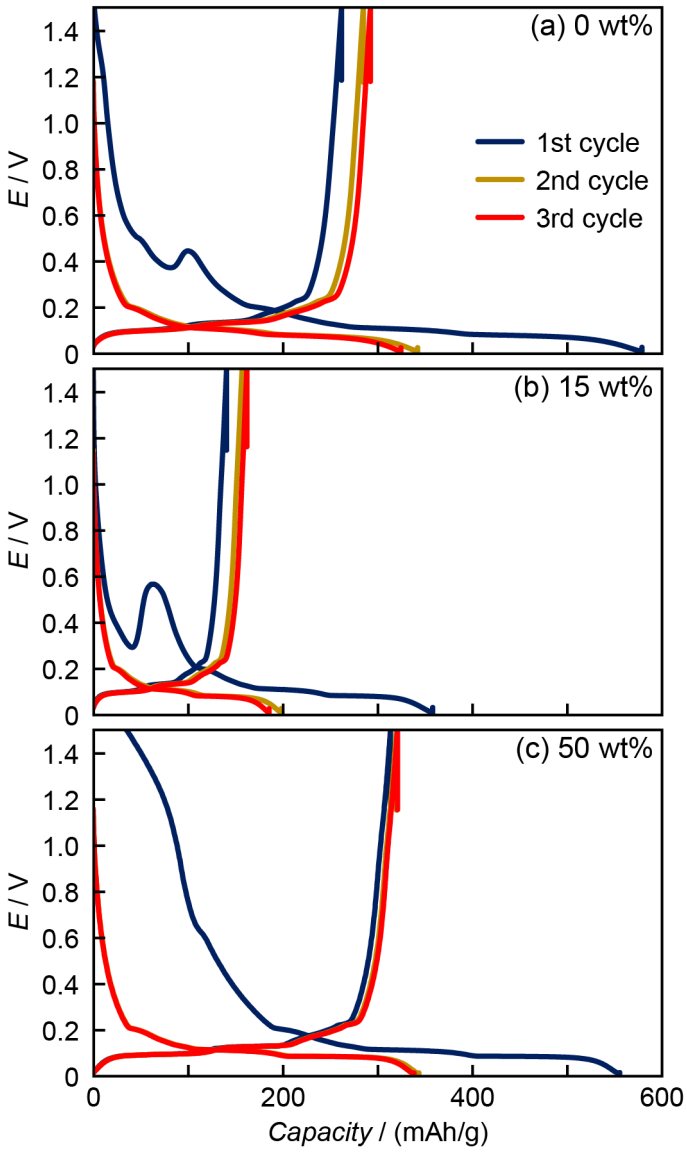

Figure S1. Charge-discharge curves for (a) the solid-state graphite anode without the [C_2mpyr][FSI] composite and the solid-state graphite-[C_2mpyr][FSI] composite anodes with (b) 15 wt% and (c) 50 wt% [C_2mpyr][FSI] composite at the first three cycles at 50 °C.

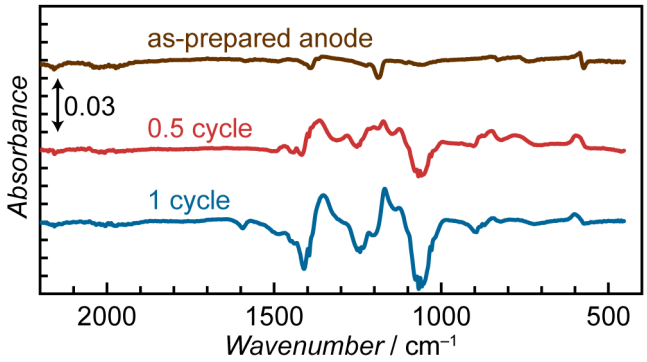

Figure S2. FTIR spectra of the as-prepared graphite-[C_2mpyr][FSI] composite anode, the graphite-[C_2mpyr][FSI] composite anode after charging to 0.005 V, and the graphite-[C_2mpyr][FSI] composite anode after one cycle.

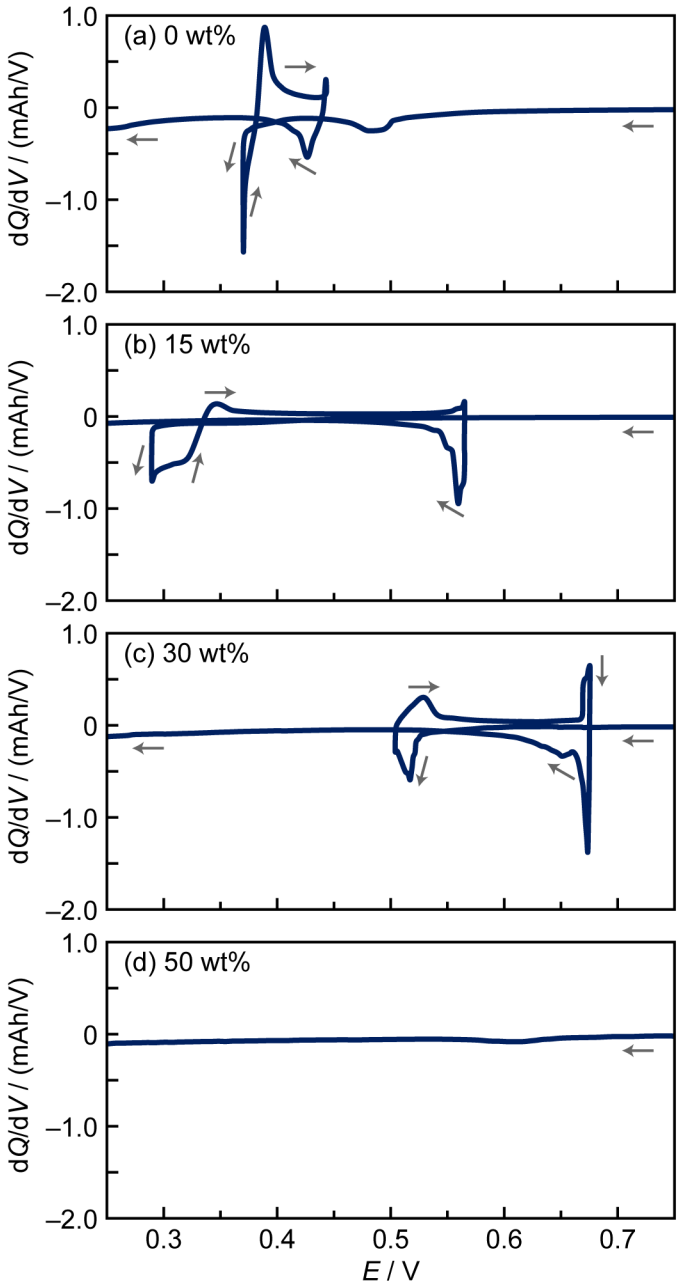

Figure S3. dQ/dV curves in the voltage range between 0.25 V and 0.75 V for (a) the solid-state graphite anode without the [C_2mpyr][FSI] composite and the solid-state graphite-[C_2mpyr][FSI] composite anodes with (b) 15 wt%, (c) 30 wt%, and (d) 50 wt% [C_2mpyr][FSI] composite at the first three cycles at 50 °C.

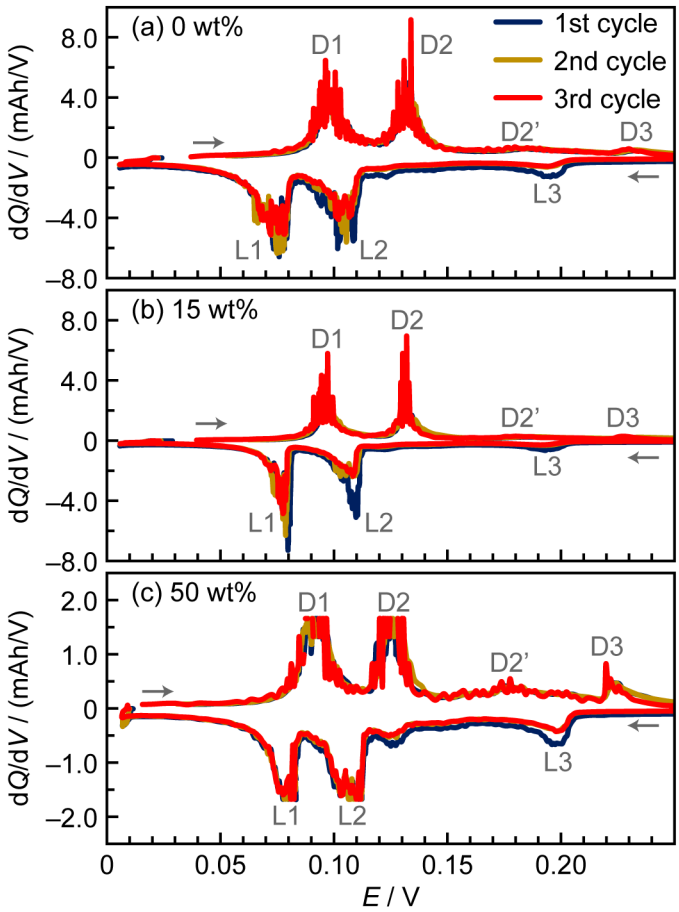

Figure S4. dQ/dV curves in the voltage range between 0 V and 0.25 V for (a) the solid-state graphite anode without the [C_2mpyr][FSI] composite and the solid-state graphite-[C_2mpyr][FSI] composite anodes with (b) 15 wt% and (c) 50 wt% [C_2mpyr][FSI] composite at the first three cycles at 50 °C.

Table S1 The peak positions of FTIR spectra for various electrolytes and their assignments.

Structure	Wavenumbers [cm^{-1}] of the peaks for			Band assignments	Ref.
	[C_2mpyr][FSI]	$Li_{0.1}$[C_2mpyr]$_{0.9}$[FSI]	10 wt% PVdF + 90 wt% $Li_{0.1}$[C_2mpyr]$_{0.9}$[FSI]		
$[FSI]^-$	1377	1377	1377	v_aSO_2	[1]
	1361	1361	1361	v_aSO_2	[1-2]
	1217	1217	1216	vSO_2-N-SO_2	[1, 3]
	1171	1170	1171	vSO_2-N-SO_2	[1, 3]
	1100	1100	1100	$v_aSO_2-N-SO_2$	[1, 3]
	826	826	826	v_aSNS, vSF	[1a, 2]
	724	724	723	v_sSNS	[1b, 2, 4]
	563	564	563	δ_aSO_2	[1b]
Pyrrolidinium ring	1032(w)	1032(w)	1031(w)	RB, vEt−N, v_aMe−N	[1b, 3, 5]
	997	998	996	Ring mode	[1b, 3]
	877(w)	877(w)	876(w)	Ring mode	[1b, 3, 6]
Others	1469	1469	1469	vCH_2, vCH_3	[1b, 6]
	1432(w)	1432(w)	1432(w)	δCH_2, δ_sCH_3	[1b, 3, 5]
	1404(sh)	1404(sh)	1398(w)	$\delta_sCH_{3(Et)}$ δ_wCH_2	[1b, 3, 5]
	936(w)	936(w)	936(w)	$v(C-C)_{Et}$	[1b, 3, 5]

The abbreviations for the band intensities and shapes: (w), weak peak; (sh) shoulder with weak intensity. The abbreviations of the vibration modes: v_a, asymmetric stretch; v_s, symmetric stretch; δ_a, asymmetric deformation (bend); δ_s, symmetric deformation

(bend); δ_w, wagging; RB, ring breathing. The abbreviations of the functional groups: Et, ethyl ($-C_2H_5$); Me, methyl ($-CH_3$).

Table S2 The peak positions of FTIR spectra for the graphite-[C_2mpyr][FSI] composite anodes (graphite anode : [C_2mpyr][FSI] composite = 70 : 30 wt%) lithiated from the open-circuit voltage to the various half-cell voltages.

Structure	Wavenumbers [cm^{-1}] of the peaks for				Band assignments	Ref.
	SE	0.6 V	0.4 V	0.1 V		
$[FSI]^-$	1377	1376(s)↓	1376	ND↓	$\nu_a SO_2$	[1]
	1361	1359↓	1359(s)	1362↓	$\nu_a SO_2$	[1-2]
	1216	1217(w)↓	1218(w)	ND↓	νSO_2-N-SO_2	[1, 3]
	1171	1169↓	1170	1171↓	νSO_2-N-SO_2	[1, 3]
	1100	1120(w)↓ ←	1117(w)	1128(w)←	$\nu_a SO_2-N-SO_2$	[1, 3]
	826	839↓←	840	849↓←	ν_aSNS, νSF	[1a, 2]
	723	749(w)↓←	754(w)←	ND↓	ν_sSNS	[1b, 2, 4]
	563	567↓←	574(w)←	595(w)←	$\delta_a SO_2$	[1b]
Pyrrolidinium ring	1031(w)	1031(w)	1032(w)	1031(w)	RB, νEt−N, ν_aMe−N	[1b, 3, 5]
	996	992↓	998	ND↓	Ring mode	[1b, 3]
	876(w)	874(w)↑	876↑	876(w)↓	Ring mode	[1b, 3, 6]
Others	1469	1468(w)↓	1468(w)	1468(w)	νCH_2, νCH_3	[1b, 6]
	1432(w)	1431(w)	1431(w)	1431(w)	δCH_2, $\delta_s CH_3$	[1b, 3, 5]
	1398(w)	1398(w)	1398(s)	1398(w)	$\delta_s CH_{3(Et)}$ $\delta_w CH_2$	[1b, 3, 5]
	ND	1279↑	1276	1280	$\nu(CF_2)_{PVdF}$, ν(C−N)?	[7]
	936(w)	938(w)↓	938(s)	ND↓	$\nu(C-C)_{Et}$	[1b, 3, 5]

SE, 10 wt% PVdF + 90 wt% $Li_{0.1}[C_2mpyr]_{0.9}[FSI]$; ND, not detected; ↑, increased; ↓, decreased; ←, blueshifted. The other footnotes are provided under Table S1.

II. Supporting artworks for the "*Charge rate performance*" section

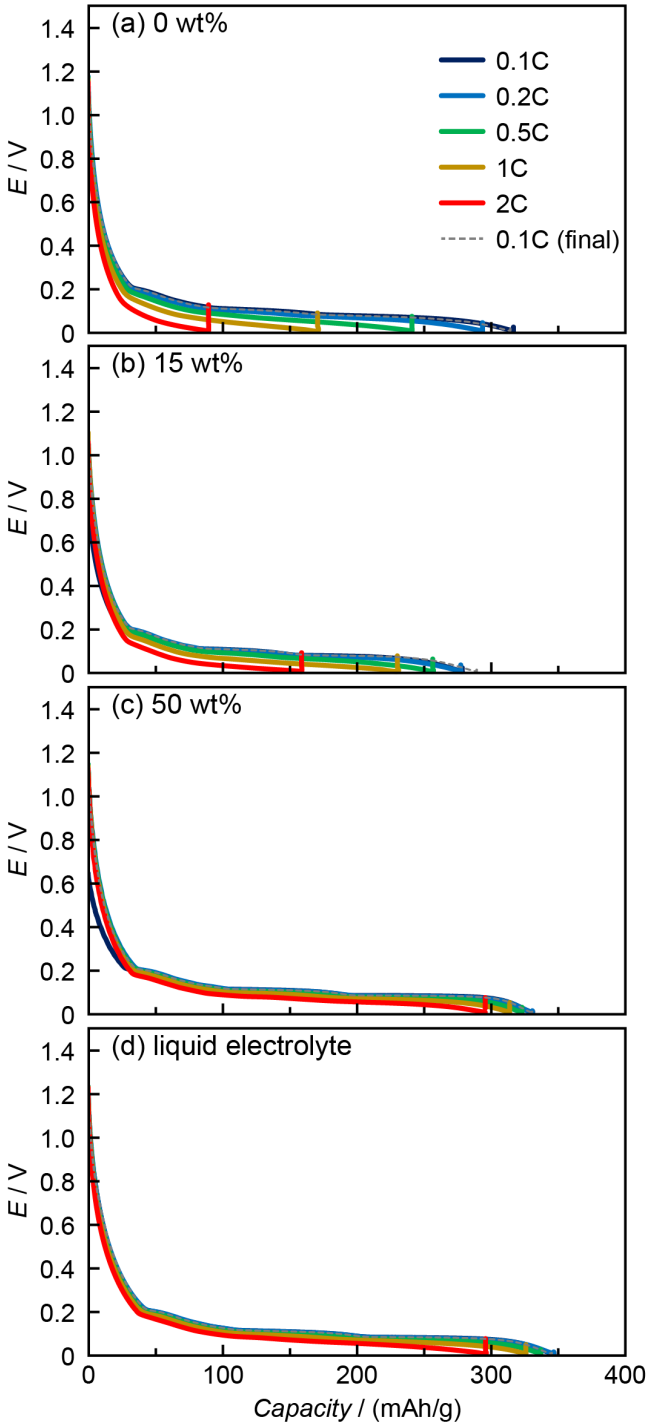

Figure S5. (a) Charge curves for (a) the solid-state graphite anode without the [C_2mpyr][FSI] composite, the solid-state graphite-[C_2mpyr][FSI] composite anodes with (b) 15 wt% and (c) 50 wt% [C_2mpyr][FSI] composite, and (d) the graphite anode with a liquid electrolyte, 1.0 M $LiPF_6$ in EC-DEC-DMC (1 : 1 : 1 volume ratio) at 50 °C.

III. Supporting artworks for the "*Cycle life*" section

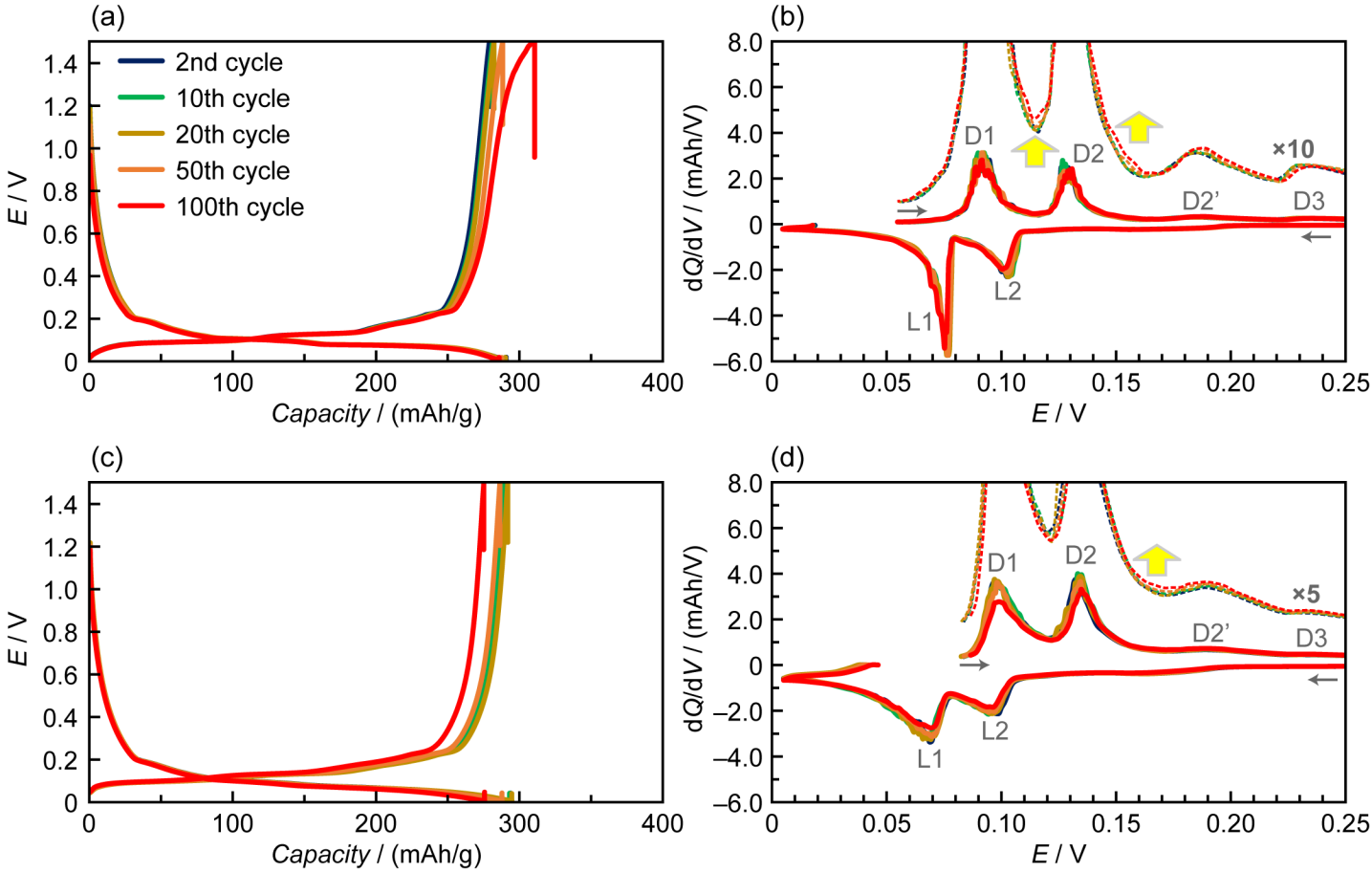

Figure S6. (a) Charge-discharge curves and (b) dQ/dV curves for the solid-state graphite-[C_2mpyr][FSI] composite anode (50 wt% graphite anode + 50 wt% [C_2mpyr][FSI] composite) at the 2nd, 10th, 20th, 50th, and 100th cycles at 50 °C. (c) Charge-discharge curves and (d) dQ/dV curves for the solid-state graphite anode at the 2nd, 10th, 20th, 50th, and 100th cycles at 50 °C.

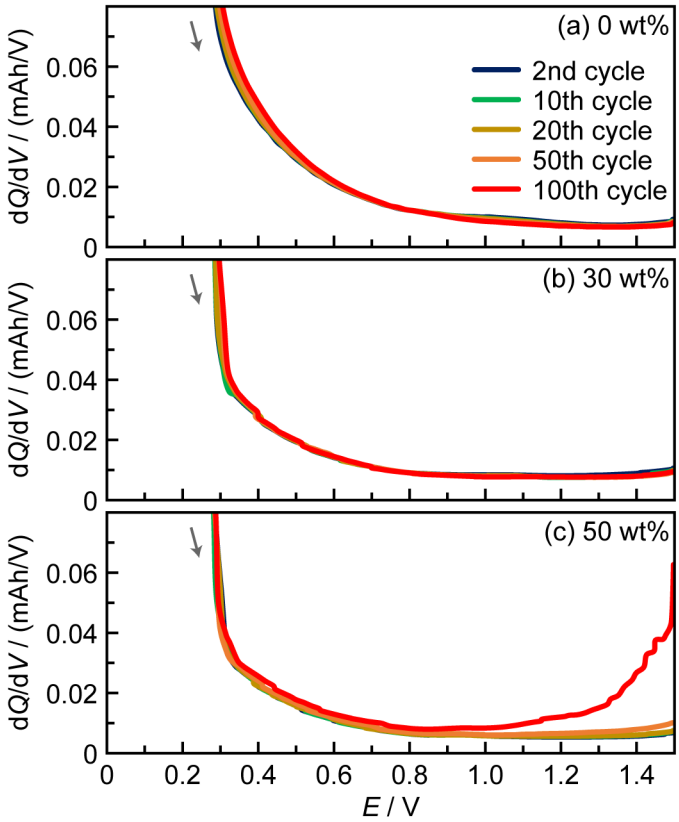

Figure S7. Enlarged dQ/dV curves for (a) the solid-state graphite anode without the [C_2mpyr][FSI] composite and the solid-state graphite-[C_2mpyr][FSI] composite anodes with (b) 30 wt% and (c) 50 wt% [C_2mpyr][FSI] composite during delithiation at the 2nd,10th, 20th, 50th, and 100th cycles at 50 °C.

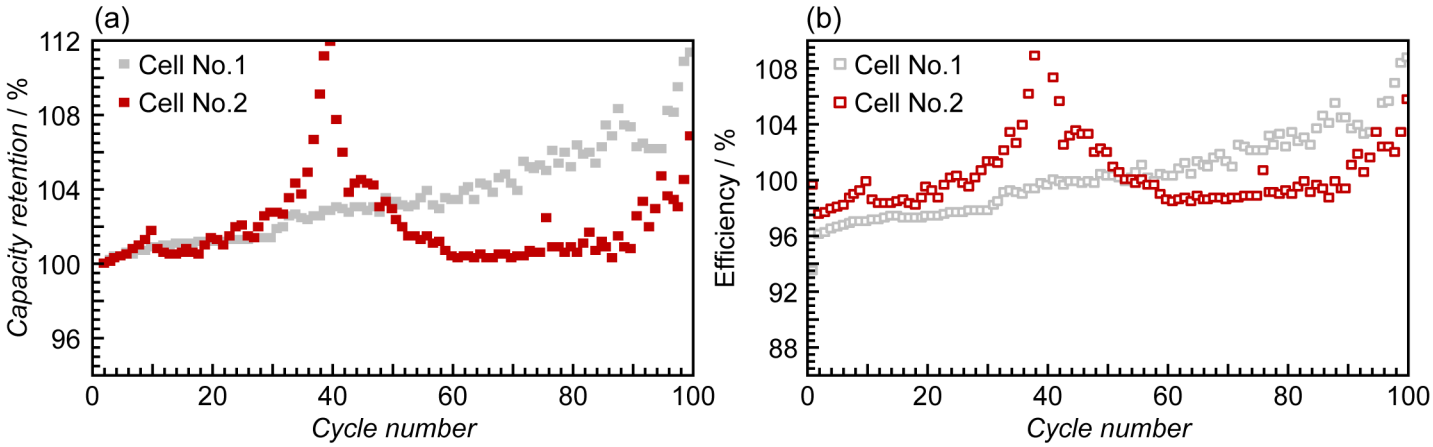

Figure S8. (a) The discharge capacity retention and (b) Coulombic efficiency for the solid-state graphite-[C_2mpyr][FSI] composite anode (50 wt% graphite anode + 50 wt% [C_2mpyr][FSI] composite) at 50 °C. (Cell No.1: The anode disk is the same as that of Figure 4c. Cell No.2: The anode disk is different from Figure 4c.)

IV. Supporting artworks for the "*Electrode structure*" section

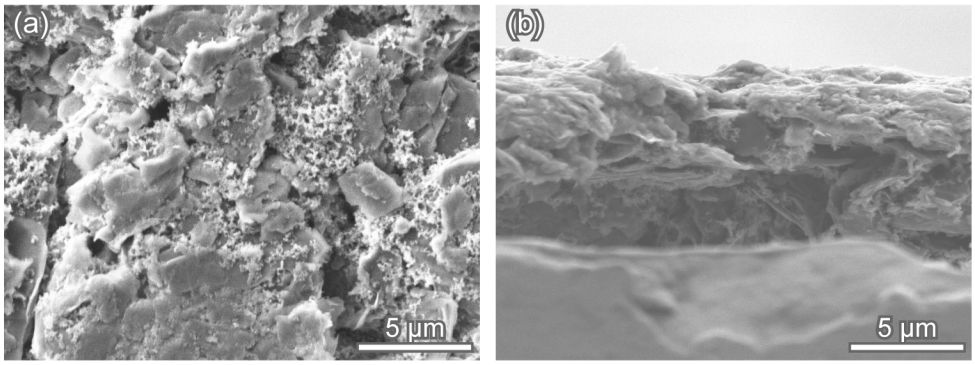

Figure S9. (a) The surface and (b) the cross-sectional SEM images of the solid-state graphite-[C_2mpyr][FSI] composite anodes with 15 wt% [C_2mpyr][FSI] composite.

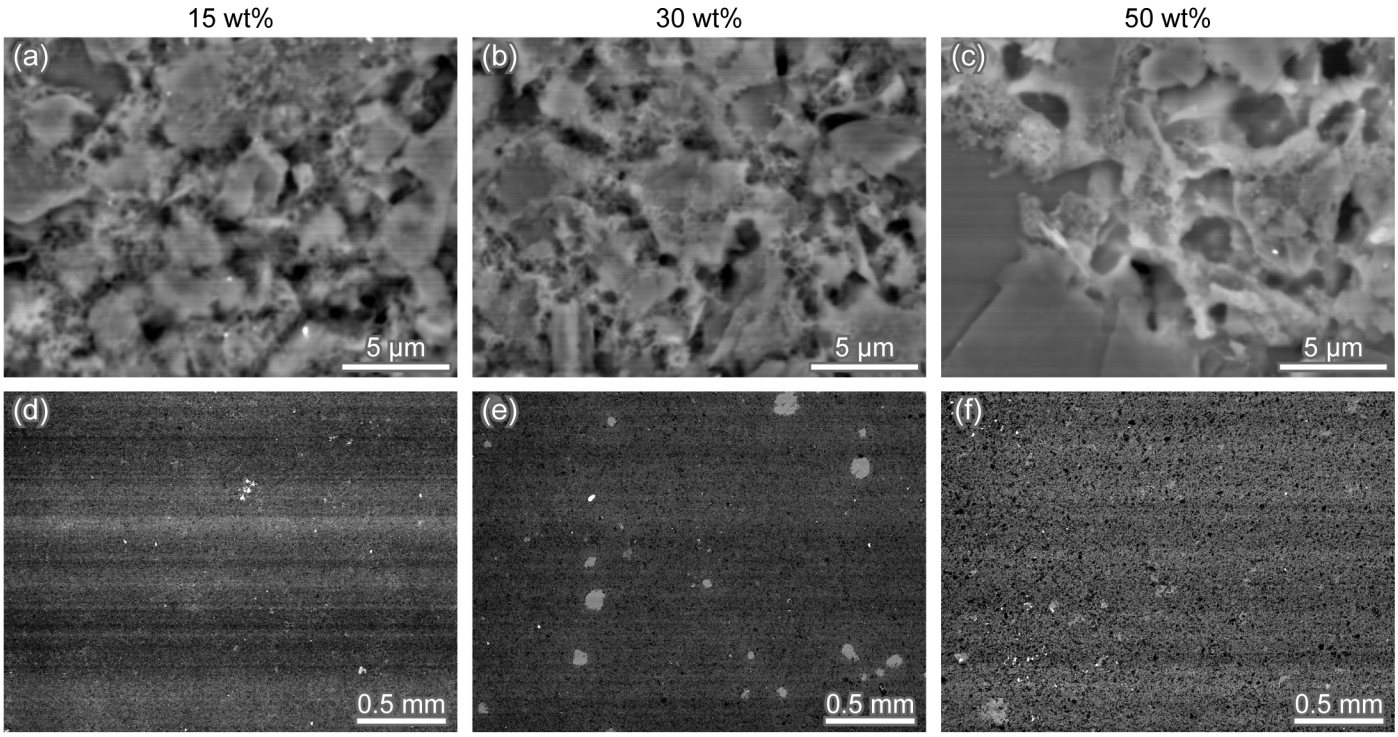

Figure S10. The BSE images for the surfaces of the solid-state graphite-[C_2mpyr][FSI] composite anodes with (a,d) 15 wt%, (b,e) 30 wt%, and (c,f) 50 wt% [C_2mpyr][FSI] composite. Magnification: (a−c) ×6,000 and (d−f) ×50.

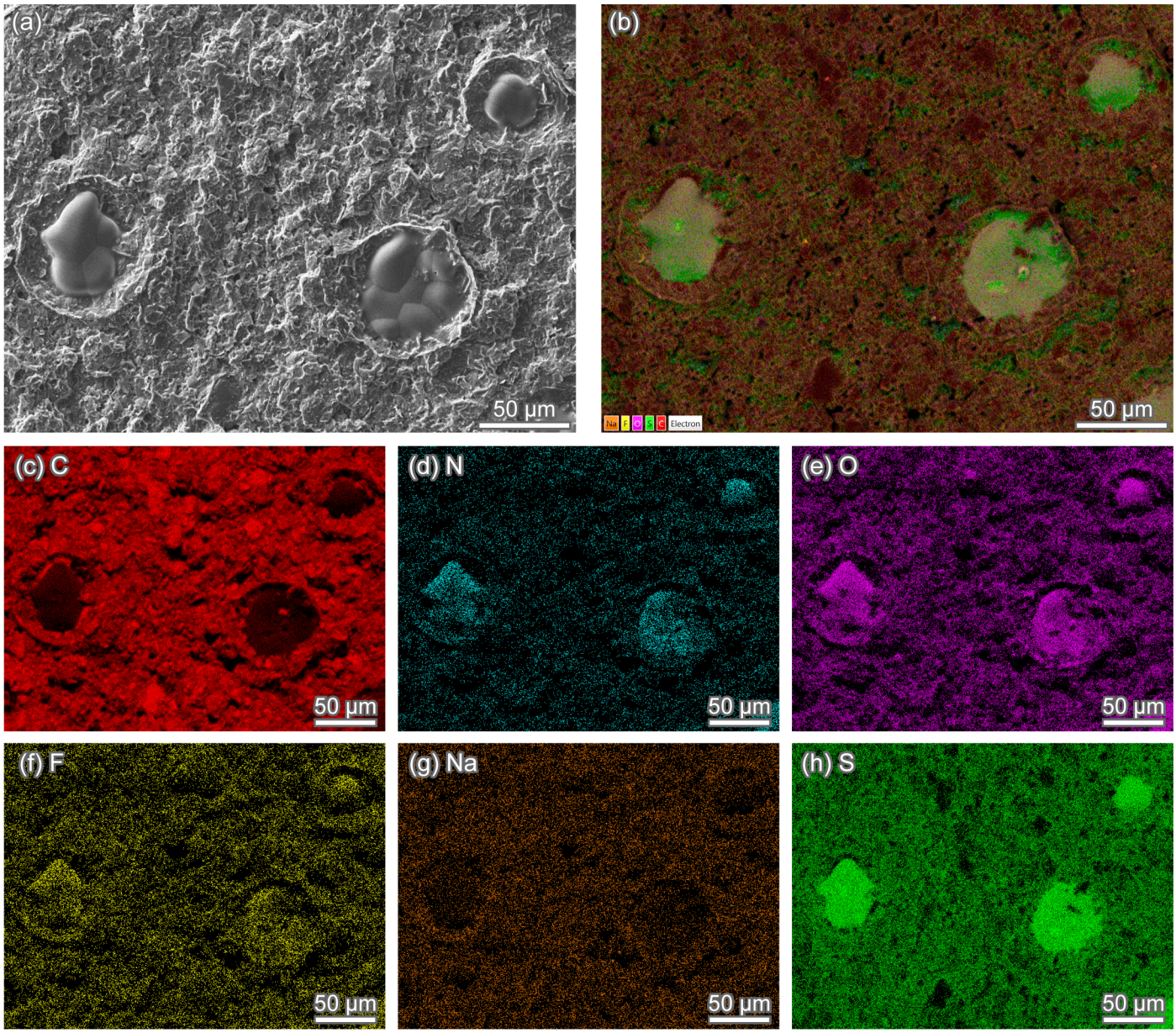

Figure S11. (a) The SEM image for the surface of the solid-state graphite-[C_2mpyr][FSI] composite anode (70 wt% graphite anode + 30 wt% [C_2mpyr][FSI] composite). (b) The layered image as a result of elemental mappings. (c) C, (d) N, (e) O, (f) F, (g) Na, and (h) S elemental mappings for the area resolved in (a).

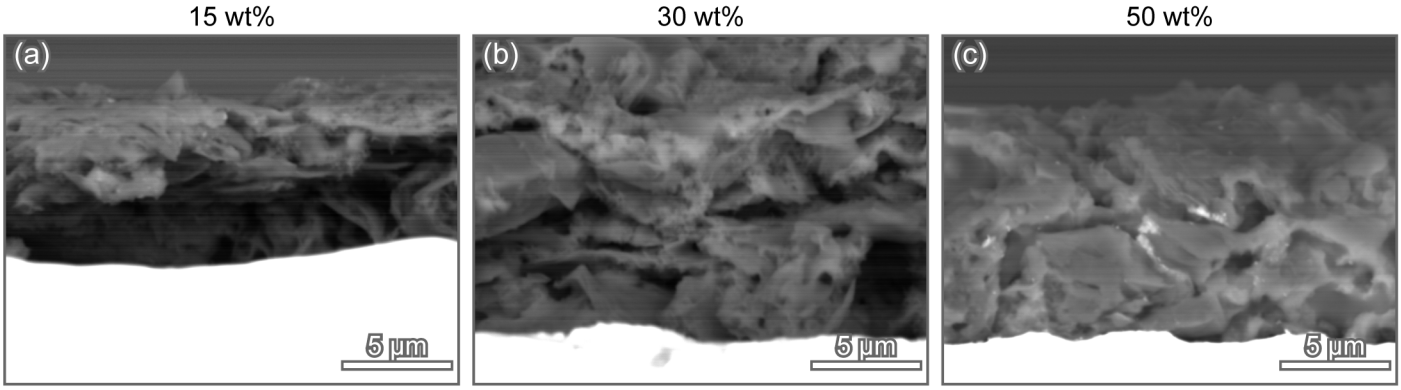

Figure S12. The BSE images for the cross-sections of the solid-state graphite-[C_2mpyr][FSI] composite anodes with (a) 15 wt%, (b) 30 wt%, and (c) 50 wt% [C_2mpyr][FSI] composite.

V. Supporting artworks for the "*EIS after the cycle test*" section

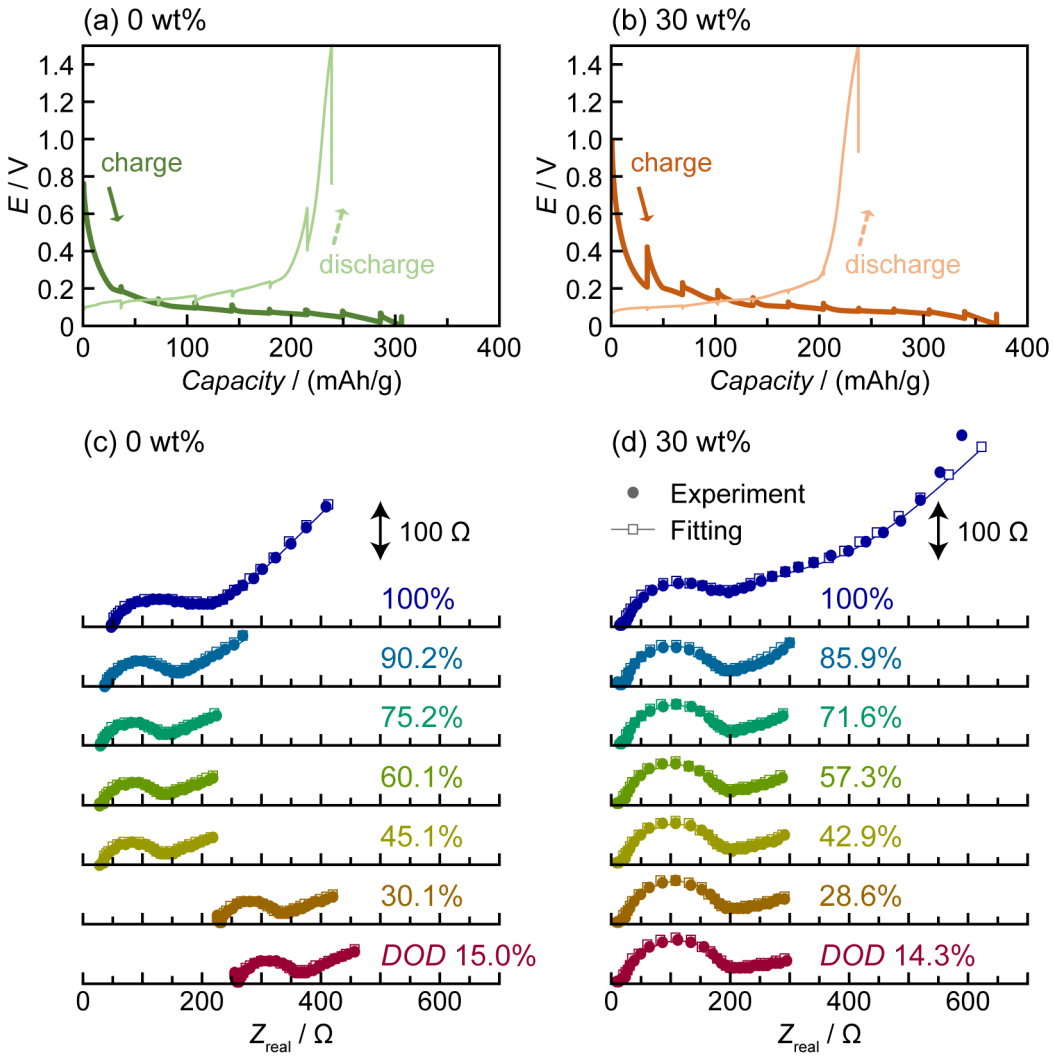

Figure S13. Charge-discharge curves for (a) the solid-state graphite anode and (b) the solid-state graphite-[C_2mpyr][FSI] composite anode (70 wt% graphite anode + 30 wt% [C_2mpyr][FSI] composite) at the 0.1C charge/discharge at 50 °C after the cycle test. Nyquist plots at various DODs at 50 °C for (c) the solid-state graphite anode and (d) the solid-state graphite-[C_2mpyr][FSI] composite anode (70 wt% graphite anode + 30 wt% [C_2mpyr][FSI] composite).

VI. Supporting artworks for Experimental Section.

Table S3 Composition, electrode loading, and density of the solid-state graphite anode disks.

Aimed graphite anode : $[C_2mpyr][FSI]$ composite ratio [wt%]	Interlayer + Electrolyte	Actual Graphite : C65 : Na-CMC : $[C_2mpyr][FSI]$: LiFSI ratio [wt%]	Electrode loading [mg/cm^2]	Electrode density [g/cm^3]	Used in
50 : 50	PVdF + $[C_2mpyr][FSI]$ composite	45.00 : 2.50 : 2.50 : 46.70 : 3.30	1.78	1.27	Figures 4c, 4d, S6a, S6b, S7c, S8a, S8b, Table 3
50 : 50	PVdF + $[C_2mpyr][FSI]$ composite	45.00 : 2.50 : 2.50 : 46.70 : 3.30	1.73	1.23	Figures S8a, S8b
50 : 50	PVdF + $[C_2mpyr][FSI]$ composite	45.00 : 2.50 : 2.50 : 46.70 : 3.30	1.73	1.23	Figures 2b, 3, S1c, S3d, S4c, S5c, Tables 1, 2
70 : 30	PVdF + $[C_2mpyr][FSI]$ composite	63.00 : 3.50 : 3.50 : 28.02 : 1.98	1.55	1.19	Figures 4a–4d, 6c–6f, S7b, S13b, S13d, Table 3
70 : 30	PVdF + $[C_2mpyr][FSI]$ composite	63.00 : 3.50 : 3.50 : 28.02 : 1.98	1.24	1.13	Figures 1a, 1e, 1f, 2a, 2b, 3, S3c, Tables 1, 2
85 : 15	PVdF + $[C_2mpyr][FSI]$ composite	76.50 : 4.25 : 4.25 : 14.01 : 0.99	1.55	1.10	Figures 3, S1b, S3b, S4b, S5b, Tables 2, S4, S5
100 : 0	PVdF + $[C_2mpyr][FSI]$ composite	90.02 : 4.99 : 5.00 : 0 : 0	1.61	1.07	Figures 2b, 3, 4c, 4d, 6b, 6d−6f, S1a, S3a, S4a, S5a, S6c, S6d, S7a, S13a, S13c, Tables 1−3
100 : 0	PP + 1 M $LiPF_6$ in EC-DEC-DMC (1 : 1 : 1 vol%)	90.02 : 4.99 : 5.00 : 0 : 0	1.69	1.40	Figures 1b, 1f, 2b, 3, S5d, Tables 1, 2

VII. Supporting discussions for the appearance of the peak in the charge-discharge profiles at the first cycle

(i) Effect of the rest time on the appearance of the peak

To obtain further insights into the appearance of the peak during the first charging, the effect of the rest time between assembling the coin cells followed by resting in a 50 °C oven and starting the lithiation process of the graphite-[C_2mpyr][FSI] composite anodes in the cells was investigated. Remarkably, the feature in the 0.4-0.7 V range disappeared for the cell rested for a longer time (see Figure S14). This implies that the side reaction that causes the appearance of the peak, which has been identified as the decomposition of PVdF in the interlayer in Section VII-(ii), is a slow process but it still occurs spontaneously without applying a negative current to the graphite-[C_2mpyr][FSI] composite anodes. Based on the evidence shown in the previous study,[8] this spontaneous reduction does possible because $[FSI]^-$ anions would reduce to $\bullet SO_2NSO_2F^-$ radical anions when $[FSI]^-$ anions have attached to lithium metal, the radicals migrate to the sites close to PVdF, and they dehydrofluorinate PVdF. Therefore, one of the reasons for the disappearance of the feature in the 0.4-0.7 V range in Figure S1c could be a longer rest time than the others (Figure 1a, S1a, and S1b).

Another reason for this could be the largest content of the [C_2mpyr][FSI] composite in the anode. As shown in Figs 1a and S1, the capacity observed from the open-circuit voltage to 0.6 V at the first charging increased with increasing the weight ratio of the [C_2mpyr][FSI] composite in the anode (except for the 15 wt% sample). This tendency suggested that, for the graphite-[C_2mpyr][FSI] composite anode with 50 wt% of the [C_2mpyr][FSI] composite, the SEI on the electrode surfaces was likely to be the most developed among the samples with different weight ratios. If so, it would be a reasonable consideration that the SEI provided a better barrier for observation of the feature in the 0.4-0.7 V range or the reaction before

reaching 0.6 V generated enough decomposition products of the OIPC (e.g. $\bullet SO_2NSO_2F^-$ radical anions) to hinder the peak formation in the 0.4-0.7 V range.

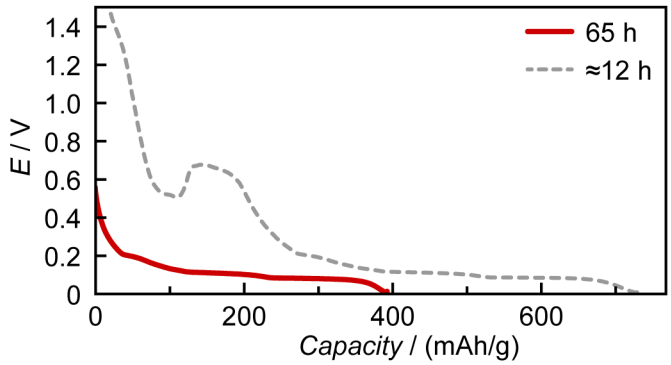

Figure S14. Charge curves for the solid-state graphite-[C_2mpyr][FSI] composite anode (70 wt% graphite anode + 30 wt% [C_2mpyr][FSI] composite) at the first cycle at 0.1C. The rest time of the half cells in a 50 °C oven before the test: overnight (ca. 12 h, dotted line) and 65 h (solid line).

(ii) Post-mortem observation and FTIR spectra analysis

The half cell of the graphite-[C_2mpyr][FSI] composite anode (70 wt% graphite anode + 30 wt% [C_2mpyr][FSI] composite) was disassembled in an Ar-filled glove box after it was charged to the voltage beyond the peak at the first charging, i.e. 0.4 V. The photo of the disassembled components is shown in Figure S15. The copper current collector was intact; no discoloration was found on its surface. In contrast, the decomposition of the interlayer, which was originally a white transparent membrane,[9] was confirmed after separating the two coin-cell spacers. Interestingly, the color change of the interlayer only occurred in the edge region where the interlayer was contacted with the two coin-cell spacers. A black substance remained in this region after disassembly. To deduce the decomposition mechanism of the interlayer, this black substance was analyzed by FTIR. Figure S16 shows the FTIR spectra of the as-prepared interlayer and the black substance. As can be seen, the shape of the FTIR spectrum of the black substance was almost identical to that of the as-prepared interlayer. However, two new features appeared for the black substance: the shoulder at around 1560 cm^{-1} and the broad peak at 2051 cm^{-1}. According to the previous study, dehydrofluorinated PVdF films show the peaks related to C=C stretching at 1552−1630 cm^{-1} and C≡C stretching at 2100−2150 cm^{-1}.[10] Therefore, it was suggested that the decomposition reaction involved PVdF in the interlayer and the product was dehydrofluorinated PVdF. A proposed mechanism of this reaction is as follows. Firstly, $[FSI]^-$ anions are decomposed to radical anions:

$$FSO_2NSO_2F^- + e^- \rightarrow \bullet SO_2NSO_2F^- + F^- \quad \text{(S1)}$$

$$FSO_2NSO_2F^- + e^- \rightarrow \bullet NSO_2F^- + SO_2F^- \quad \text{(S2)}$$

Secondly, the radical anions ($\bullet A^-$) dehydrate and defluorinate PVdF:

$$-CH_2-CF_2- + \bullet A^- \rightarrow -\bullet CH-CF_2- + HA^- \quad \text{(S3)}$$

$$-CH_2-CF_2- + \bullet A^- \rightarrow -CH_2-\bullet CF- + FA^- \quad \text{(S4)}$$

Finally, the radicals in a polymer chain meet each other to form C=C double bonds:

$$-(\bullet CH-CF_2- \ldots -CH_2-\bullet CF)- \rightarrow -(CH=CF- \ldots -CH_2-CF_2)- \quad \text{(S5)}$$

The formation of C≡C triple bonds can be described in a similar fashion. Eq. (S1) can be initiated when $[FSI]^-$ anions are contacted with lithium metal[8, 11] or are electrochemically reduced.[12] Although Eq. (S1) is reportedly a more dominant reaction than Eq. (S2), $\bullet SO_2NSO_2F^-$ is not prone to abstract a hydrogen atom in C–H bonds.[11] Therefore, it is tentatively concluded that $\bullet NSO_2F^-$ is the most probable species to initiate Eq. (S3). The post-mortem observation and FTIR analysis of the black substance derived from the interlayer and a further FTIR analysis of the solid-state graphite-[C_2mpyr][FSI] composite anodes discussed in the "*Initial charge-discharge profile*" section suggest that the origin of the peak during the first charging is likely to be the dehydrofluorination of PVdF in the interlayer periphery rather than the SEI formation stemming from the reduction of [C_2mpyr][FSI].

Figure S15. The photo of the components after charging to 0.4 V.

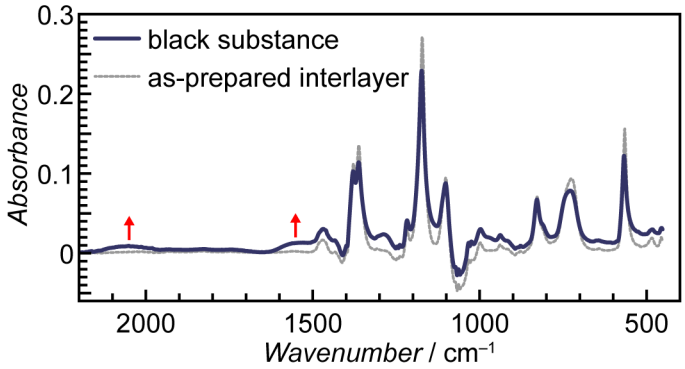

Figure S16. The FTIR spectra of the black substance (solid line) and the as-prepared interlayer (dotted line).

VIII. Supporting discussions for the data set of the 15wt% samples

(i) Coulombic efficiencies and discharge capacities at the first three cycles

Table S4 shows capacities and Coulombic efficiencies for the solid-state graphite-[C_2mpyr][FSI] composite anodes with the OIPC composite ratio of 15wt%. Notably, the first Coulombic efficiency depends on the OIPC composite ratio inside a graphite anode. As the inside OIPC composite ratio increases from 0 to 30 wt%, the first Coulombic efficiency decreases, but a further increase in the OIPC composite ratio (to 50 wt%) improves the first Coulombic efficiency. As for the discharge capacity, while the graphite anode with the liquid electrolyte indicates 338.1 mAh/g at the third cycle, lower third discharge capacities are measured for the solid-state graphite-[C_2mpyr][FSI] composite anodes, which depends on the OIPC composite ratio as well. The solid-state graphite-[C_2mpyr][FSI] composite anode with 15 wt% OIPC composite shows the lowest third discharge capacity (161.8 mAh/g). In contrast, the highest third discharge capacity is found for the anode with 50 wt% OIPC composite (320.5 mAh/g). Dependency on the OIPC composite ratio inside a graphite anode can be explained as follows: Firstly, small additions of the OIPC composite into a graphite anode would generate disturbance layers between graphite particles. The layers are the OIPC composite grains that are separated from the bulk OIPC composite (in the anode and the PVdF fiber) and hamper Li^+ diffusion from one graphite particle to another via the separated OIPC composite grains (Figure S17). Because the solid-state graphite anode without the OIPC composite shows a higher capacity than that with a small amount of the OIPC composite (15 wt%), it can be said that Li^+ diffusion between graphite particles is more favorable than that through the two interfaces of graphite | [C_2mpyr][FSI] + LiFSI (90 : 10 mol%) | graphite. Therefore, a small addition of the OIPC composite might impose unfavorable Li^+ conduction paths on some graphite particles and make them inactive during cycling, decreasing the achievable capacity of the solid-state

graphite-[C_2mpyr][FSI] composite anode. Secondly, further addition of the OIPC composite would connect separated OIPC composite grains to the bulk one and, thus, reduces the amount of inactivated graphite particles. This effect appears as the improvement of the capacity after the addition of the OIPC composite from 15 to 30 wt%. Thirdly, the discharge capacity improvement can be enhanced by an additional increase in the OIPC composite ratio from 30 to 50 wt%. Most of all graphite particles might be accessible with an extra amount of the OIPC composite inside the anode, where OIPC composite grains are connected well with each other and provide graphite particles with sufficient Li^+ conduction pathways to/from the bulk OIPC composite. Indeed, the anode with 50 wt% OIPC composite reaches 320.5 mAh/g at the third cycle, which is close to the capacity observed for the anode with proper electrolyte/active material connections using the liquid electrolyte (338.1 mAh/g). Hence, the large addition of the OIPC composite (>30 wt%) into a graphite anode is advantageous in terms of the charge-discharge performance for the first three cycles.

Table S4 Charge and discharge capacities and Coulombic efficiencies at the first three cycles for the solid-state graphite-[C_2mpyr][FSI] composite anodes (85 wt% graphite anode + 15 wt% [C_2mpyr][FSI] composite).

Graphite anode : [C_2mpyr][FSI] composite [wt%]	Interlayer + Electrolyte	Cycle number	Charge capacity [mAh/g]	Discharge capacity [mAh/g]	Efficiency [%]
85 : 15	PVdF + [C_2mpyr][FSI] composite	1	357.5	140.4	39.3
		2	198.2	156.8	79.1
		3	185.2	161.8	87.4

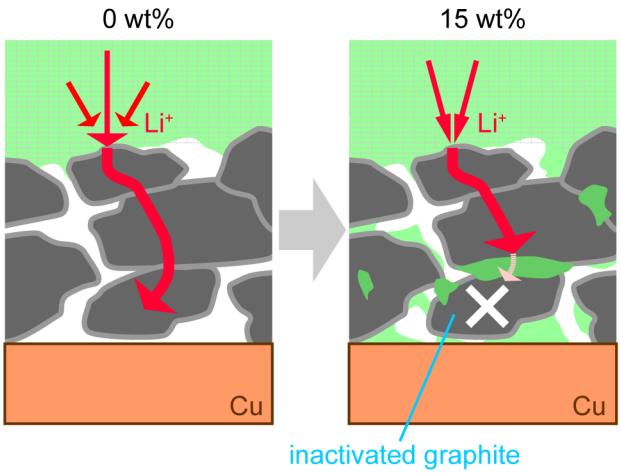

Figure S17 The schematic illustration of the solid-state graphite anode and some graphite particles inactivated by the addition of the [C_2mpyr][FSI] composite (the OIPC composite ratio inside the anode: 0 wt% to 15 wt%).

(ii) Charge rate capability

Table S5 shows the charge capacity and capacity ratio at each charge C-rate for the solid-state graphite-[C_2mpyr][FSI] composite anodes with the OIPC composite ratio of 15wt%. All charge capacities were lower than those for the other solid-state graphite-[C_2mpyr][FSI] composite anodes and the solid-state graphite anode without the [C_2mpyr][FSI] composite at the same charge C-rate. As stated previously, this is likely to be attributed to disturbance layers (i.e. OIPC composite grains separated from the bulk OIPC composite) between graphite particles. However, the capacity ratio of the 15wt% sample was evaluated to be between those of the 0wt% and 30wt% samples at the same charge C-rate. The addition of the OIPC composite in the graphite anode improved the charge rate capability of its half cell.

Table S5 Charge rate capability for the solid-state graphite-[C_2mpyr][FSI] composite anodes (85 wt% graphite anode + 15 wt% [C_2mpyr][FSI] composite).

Graphite anode : [C_2mpyr][FSI] composite [wt%]	Interlayer + Electrolyte	C-rate	Charge capacity [mAh/g]	Capacity ratio [%]
85 : 15	PVdF + [C_2mpyr][FSI] composite	0.1C	174.1	96.3
		0.2C	173.4	95.9
		0.5C	160.4	88.7
		1C	143.9	79.6
		2C	99.3	54.9
		0.1C (final)	180.8	100

IX. Supporting discussions for the relatively low volume fraction of the electrolyte for the graphite-[C_2mpyr][FSI] composite anode

As shown in Figure 3, the amount of the electrolyte required for the solid-state graphite-[C_2mpyr][FSI] composite anode to achieve a certain level of the charge rate capability is smaller than that for the solid-state graphite anode with the liquid electrolyte. A possible reason for the relatively low amount of the electrolyte in the OIPC composite is the presence of liquid phases inside the OIPC composite, which are likely to be generated during charging/discharging.

To get some insights into this, firstly, the amount of lithium ions required to fully lithiate graphite and that in the PVdF fiber with the OIPC composite were calculated. If the capacity is 0.246 mAh (estimated based on the active material ratio and the loading of the solid-state graphite anode without the OIPC composite in Table S3 and the capacity of graphite, 340 mAh/g), dividing this value by the Faraday constant (96,485 A s mol^{-1}) provides the amount of Li^+ ions for the full lithiation of graphite (9.2×10^{-6} mol). However, the amount of lithium ions in the PVdF fiber is 2.0×10^{-6} mol (using the thickness of the PVdF fiber: 100 μm, the area of the PVdF fiber: 0.503 cm^2, and the tabulated information in Table S6). This means many lithium ions come from lithium metal during charging.

Table S6 The molecular weight (M_i), density (d_i), and concentration (C_i) of the material *i* and the mass fraction ($w_{i,\mathrm{PVdF}}$), volume fraction ($\varphi_{i,\mathrm{PVdF}}$), and concentration ($C_{i,\mathrm{PVdF}}$) of the material *i* in the PVdF fiber with the [C_2mpyr][FSI] composite (PVdF : [C_2mpyr][FSI] composite = 90 : 10 wt% and [C_2mpyr][FSI] : LiFSI = 90 : 10 mol%).

Name	M_i [g/mol]	d_i [g/cm^3]	C_i [M]	$w_{i,\mathrm{PVdF}}$ [wt%]	$\varphi_{i,\mathrm{PVdF}}$ [%]	$C_{i,\mathrm{PVdF}}$ [M]
[C_2mpyr][FSI]	294.34	1.2	4.1	84.1	88.7	3.6
LiFSI	187.07	2.32	12	5.9	3.2	0.40
PVdF	534,000	1.74	3.26×10^{-3}	10.0	8.1	2.6×10^{-3}

Next, the feasibility of lithium-ion diffusion from the lithium metal to the solid-state graphite anode in the time scale of charging was evaluated. According to the literature, the PVdF fiber with the [C_2mpyr][FSI] composite shows an ionic conductivity (σ_{total}) of 1.80×10^{-5} S cm^{-1}.[9] From Table S6, the total concentration of ionic moieties is 4.0 M. Dividing σ_{total} by this value gives the molar conductivity of the PVdF fiber with the [C_2mpyr][FSI] composite (Λ_{total}), 4.5×10^{-7} S m^2 mol^{-1}. The molar conductivity of lithium ions ($\Lambda_{\mathrm{Li^+}}$) can be calculated by the following equation:

$$\Lambda_{\mathrm{Li^+}} = t_{\mathrm{Li^+}}\Lambda_{\mathrm{total}} / (x_{\mathrm{Li^+,composite}}/100) \quad \text{(S6)}$$

where $t_{\mathrm{Li^+}}$ is the lithium transport number of the PVdF fiber with the [C_2mpyr][FSI] composite (0.1)[9] and $x_{\mathrm{Li^+,composite}}$ is the mole fraction of lithium ions in the [C_2mpyr][FSI] composite (90 mol%). $\Lambda_{\mathrm{Li^+}}$ was estimated to be 4.5×10^{-7} S m^2 mol^{-1}. Then, the diffusion coefficient of lithium ions can be obtained from the Nernst-Einstein equation:

$$\Lambda_{\mathrm{Li^+}} = z_{\mathrm{Li^+}}{}^2F^2D_{\mathrm{Li^+}}/(RT) \quad \text{(S7)}$$

where $z_{\mathrm{Li^+}}$ is the charge of lithium ions (+1), F is the Faraday constant (96,485 A s mol^{-1}), R is the gas constant (8.314 J K^{-1} mol^{-1}), and T is the temperature in Kelvin (323.15 K). By Eq. (S7),

D_{Li^+} was estimated to be 1.3×10^{-13} m^2 s^{-1}. The diffusion length of lithium ions in the time scale of charging (L_{Li^+} [μm]) can be evaluated using Eq. (S8):[13]

$$L_{Li^+} = (2D_{Li^+}t)^{1/2} / 10^6 \quad \text{(S8)}$$

Table S5 shows L_{Li^+} after various charge times. Note that all L_{Li^+} values are less than the thickness of the PVdF fiber with the [C_2mpyr][FSI] composite, 100 μm. This implies if the [C_2mpyr][FSI] composite only has the solid phase during charging, lithium ions generated at the lithium metal cannot diffuse to the graphite anode within 36,000 s. If the presence of liquid phases is assumed, L_{Li^+} will be ca. 10-fold higher than those shown in Table S7 because the σ_{total} value of the liquid [C_2mpyr][FSI] composite is two orders of magnitude higher than that of the solid [C_2mpyr][FSI] composite.[14] In this case, L_{Li^+} is expected to be >100 μm within 36,000 s and the migration of generated lithium ions from one side to another becomes possible.

Table S7 L_{Li^+} after various charge times.

C-rate	*t* [s]	L_{Li^+} [μm]
0.1	36,000	96.5
0.2	18,000	68.2
0.5	7,200	43.1
1	3,600	30.5
2	1,800	21.6

X. Supporting discussions for the fluctuation in the discharge capacity retention and Coulombic efficiency for the 50wt% sample

As discussed in Section VII-(ii), dehydrofluorination of PVdF is a side reaction that could occur during cycling. At the very beginning of cell cycling, the edge of the interlayer decomposed to a black substance (see the photo in Figure S15), which could be a partly dehydrofluorinated PVdF. As the cycle number increases, this degradation would spread through the interlayer and make it partly electron-conductive because of a relatively higher electronic conductivity of dehydrofluorinated PVdF ($<10^{-7}$ S cm^{-1})[10] than that of pure PVdF (ca. 10^{-13} S cm^{-1}).[15] This could be a possible reason for the fluctuation in the discharge capacity retention and efficiency. As the electron-conduction pathway through dehydrofluorinated PVdF changes along with the pressure coming from the surrounding materials (e.g. volume expansion and shrinkage of graphite particles), the "actual" electronic conductivity ($\sigma_{e,actual}$) of the interlayer is subject to fluctuation. If $\sigma_{e,actual}$ is higher than that at the previous cycle, more intense spontaneous lithiation occurs in a high voltage range (i.e. 1.0−1.5 V), and the larger discharge capacity is measured. Because $\sigma_{e,actual}$ was not stable, the fluctuation in the discharge capacity retention and efficiency was observed.

XI. References

[1] a) L. Li, S. Zhou, H. Han, H. Li, J. Nie, M. Armand, Z. Zhou, X. Huang, *J. Electrochem. Soc.* **2011**, *158*, A74−A82; b) P. C. Howlett, N. Brack, A. F. Hollenkamp, M. Forsyth, D. R. MacFarlane, *J. Electrochem. Soc.* **2006**, *153*, A595−A606.

[2] N. B. Colthup, L. H. Daly, S. E. Wiberley, in *Introduction to Infrared and Raman Spectroscopy (Third Edition)* (Eds.: N. B. Colthup, L. H. Daly, S. E. Wiberley), Academic Press, San Diego, **1990**, pp. 355−385.

[3] B. Bednarska-Bolek, R. Jakubas, G. Bator, J. Baran, *J. Mol. Struct.* **2002**, *614*, 151−157.

[4] I. Rey, J. C. Lassègues, J. Grondin, L. Servant, *Electrochim. Acta* **1998**, *43*, 1505−1510.

[5] S. A. Katsyuba, P. J. Dyson, E. E. Vandyukova, A. V. Chernova, A. Vidi, *Helv. Chim. Acta* **2004**, *87*, 2556−2565.

[6] J. Adebahr, P. Johansson, P. Jacobsson, D. R. MacFarlane, M. Forsyth, *Electrochim. Acta* **2003**, *48*, 2283−2289.

[7] a) D. Suhendra, E. R. Gunawan, L. Kusumawati, *Rasayan J. Chem.* **2019**, *12*, 765−772; b) P. Nallasamy, S. Mohan, *Indian J. Pure Appl. Phys.* **2005**, *43*, 821−827.

[8] A. Basile, A. I. Bhatt, A. P. O'Mullane, *Nat. Commun.* **2016**, *7*, 11794.

[9] Y. Zhou, X. Wang, H. Zhu, M. Armand, M. Forsyth, G. W. Greene, J. M. Pringle, P. C. Howlett, *Phys. Chem. Chem. Phys.* **2017**, *19*, 2225−2234.

[10] H. Kise, H. Ogata, M. Nakata, *Angew. Makromol. Chem.* **1989**, *168*, 205−216.

[11] I. A. Shkrob, T. W. Marin, Y. Zhu, D. P. Abraham, *J. Phys. Chem. C* **2014**, *118*, 19661−19671.

[12] G. M. A. Girard, M. Hilder, N. Dupre, D. Guyomard, D. Nucciarone, K. Whitbread, S. Zavorine, M. Moser, M. Forsyth, D. R. MacFarlane, P. C. Howlett, *ACS Appl. Mater. Interfaces* **2018**, *10*, 6719−6729.

[13] P. Gründler, *In-situ Thermoelectrochemistry Working with Heated Electrodes (First edition)*, Springer-Verlag Berlin Heidelberg, **2015**.

[14] Y. Zhou, X. Wang, H. Zhu, M. Yoshizawa-Fujita, Y. Miyachi, M. Armand, M. Forsyth, G. W. Greene, J. M. Pringle, P. C. Howlett, *ChemSusChem* **2017**, *10*, 3135−3145.

[15] Y. Ji, Y. Jiang, *Appl. Phys. Lett.* **2006**, *89*, 221103.